TOPEX/Poseidon observations of mesoscale eddies over the Subtropical Countercurrent: Kinematic characteristics of an anticyclonic eddy and a cyclonic eddy

Cheinway Hwang
Department of Civil Engineering, National Chiao Tung University, Hsinchu, Taiwan

Chau-Ron Wu
Department of Earth Sciences, National Taiwan Normal University, Taipei, Taiwan

Ricky Kao[1]
Department of Civil Engineering, National Chiao Tung University, Hsinchu, Taiwan

Received 30 June 2003; revised 27 September 2003; accepted 16 March 2004; published 17 August 2004.

[1] Relative dynamic heights and geostrophic fields were derived from TOPEX/Poseidon altimetry data and then used to track mesoscale eddies over the Subtropical Countercurrent (STCC). The radii, centers, vorticities, shearing deformation rates, stretching deformation rates, divergences, and center velocities of all identified eddies over the STCC were determined using a model that assumes constant velocity gradients. Most eddies are concentrated in a zonal band near 22°N, and there is an interannual variation in the number of eddies. A case study was made for a cyclonic eddy and an anticyclonic eddy, with time series of eddy kinematic parameters computed. Both eddies survive for ~220 days and propagate westward along over 22°N–24°N to reach the Kuroshio Current east coast of Taiwan, where the eddies were dissipated and in turn affected the Kuroshio Current in many ways. Sea surface temperature data and drifter data confirm the existence of these two eddies. The radii of both eddies vary and their shapes are mostly elliptical during propagation. The anticyclonic eddy propagated almost westward with oscillating north-south components, and the mean speed is 8.3 km/day. The cyclonic eddy moved southwestward before reaching 130°E and then moved northwestward, with a mean speed of 7.6 km/day. The propagations of these two eddies are basically consistent with the standard theory of eddy propagation but with larger speeds. The propagating direction could be altered while passing steep bottom topography or merging with the other eddies. *INDEX TERMS:* 4520 Oceanography: Physical: Eddies and mesoscale processes; 4576 Oceanography: Physical: Western boundary currents; 4512 Oceanography: Physical: Currents; 4594 Oceanography: Physical: Instruments and techniques; 4556 Oceanography: Physical: Sea level variations; *KEYWORDS:* mesoscale eddies, Subtropical Countercurrent, TOPEX/Poseidon

Citation: Hwang, C., C.-R. Wu, and R. Kao (2004), TOPEX/Poseidon observations of mesoscale eddies over the Subtropical Countercurrent: Kinematic characteristics of an anticyclonic eddy and a cyclonic eddy, *J. Geophys. Res.*, *109*, C08013, doi:10.1029/2003JC002026.

1. Introduction

[2] In the western Pacific the Subtropical Countercurrent (STCC) generates a productive eddy field due largely to baroclinic instability [*Qiu*, 1999]. The resulting mesoscale eddies propagate westward [e.g., *Cushman-Roisin et al.*, 1990], mostly reaching the continental shelf of the western Pacific, especially east of Taiwan. Before dissipating, these eddies interact with the Kuroshio Current, thereby modulating its volume transport and path [*Yang*, 1999; *Zhang et al.*, 2001; *Johns et al.*, 2001]. While the kinetic energy of eddies and sea surface variability in the subtropical western Pacific have been investigated extensively with altimetry by, e.g., *Qiu and Lukas* [1996], *Qiu* [1999], *Kobashi and Kawamura* [2002] and *Qiu* [2002], the propagations and evolutions of eddies in this region have not been studied in detail. The activity of eddies over the STCC has significant consequence on the dynamics of the Kuroshio upstream, and there is tremendous interest in understanding the interaction between eddy and the Kuroshio here. A case study of eddy-Kuroshio interaction near Japan has been made by *Takuji et al.* [2002]. With this understanding, scientists from Taiwan have initiated a joint project called

[1]Now at National Space Program Office, Hsinchu, Taiwan.

Copyright 2004 by the American Geophysical Union.
0148-0227/04/2003JC002026

Kuroshio Upstream Dynamics Experiment (KUDEX) to collect in-situ and satellite data and to develop numerical models to see the eddy-Kuroshio interaction in the Kuroshio upstream area, or the KUDEX area. Other topics to be included in the KUDEX research are, among others, the mechanism of water exchange between the Kuroshio and the South China Sea [e.g., *Chu and Li*, 2000]. In this project, the KUDEX area covers an area over 17°N–23°N and 119°E–130°E and has a large overlap with STCC. In this paper, the studied area covers the entire KUDEX with extension to an area over 10°N–25°N and 120°E–140°E. For convenience, this extended area is designated as STCC.

[3] Within the framework of KUDEX, this paper will focus on identifying eddies and deriving the kinematic properties of eddies using TOPEX/Poseidon (T/P) altimeter data. The existence of T/P-derived eddies will be verified by drifter data and temperature data. Methods to identify eddies from satellite data have been documented in many publications, e.g., *Meyers and Basu* [1999], *Andrade and Barton* [2000], and *Okkonen* [2001]. A complete review of eddy hydrodynamical modeling is given by *Carton* [2001]. Models for describing the kinematics of eddies can be found in, e.g., *Okubo and Ebbesmeyer* [1976], *Kirwan et al.* [1984], and *Hwang and Chen* [2000a].

[4] An overview of the T/P mission can be found in the work of *Fu et al.* [1994]. The book by *Fu and Cazenave* [2001] details all the necessary techniques in altimeter data processing and applications of altimetry in earth sciences. The T/P data used in this paper are from *Archivings Validation and Interpretation of Satellite Oceanographic Data* (*AVISO*) [1996] and the algorithm of the T/P data processing is largely based on that given in *Hwang and Chen* [2000a], so it will not be repeated here. This paper will focus on the observations of eddies and on the computations of their kinematic parameters, with only a minor emphasis on interpreting their origins and mechanisms.

2. Dynamic Height and Geostrophic Velocity From TOPEX/Poseidon Altimetry

[5] In order to track eddies over the STCC, we first computed relative dynamic heights from T/P sea surface height (SSH) data. Because the steric anomaly in the open oceans consists of mainly long wavelength components and because we intend to identify only mesoscale eddies, sea level anomaly (SLA), defined as the difference between instantaneous SSH (without tidal effects) and a mean SSH, can be regarded as relative dynamic height; see also the discussion in the work of *Wunsch and Stammer* [1998]. Considering only the balance between pressure gradient and Coriolis force, the geostrophic velocity components can be derived from the gradients of dynamic heights as:

$$u = -\frac{g}{f}\frac{\partial \zeta}{\partial y} = -\frac{g}{f}\frac{\partial \zeta}{R\partial \phi} \tag{1}$$

$$v = \frac{g}{f}\frac{\partial \zeta}{\partial x} = \frac{g}{f}\frac{\partial \zeta}{R\cos\phi\partial \lambda} \tag{2}$$

where u, v are the west-east and north-south components of velocities, ζ is the relative dynamic height, g is gravity ($\approx$9.8 m sec^{-2}), ϕ, λ are latitude and longitude, $f = 2\Omega \sin\phi$ with $\Omega \approx 7.29115 \times 10^{-5}$ s^{-1}, and R is the mean earth radius ($\approx$6371 km). In using (1) and (2) for deriving eddy velocities, the effects of centrifugal force and frictions are neglected, and this is valid for a vortex of large size (radius more than 100 km) [compare *Cushman-Roisin*, 1994]. Using (1) and (2) we have computed the geostrophic velocity fields over the STCC at each T/P cycle up to early 2002. In the computations the two gradient components of dynamic height needed in (1) and (2) were obtained by first fitting a second-degree polynomial to gridded dynamic heights, and then evaluating the differentiations using the derivatives of the polynomials. The dynamic gridded dynamic heights were computed using the minimum curvature module in the GMT package [*Wessel and Smith*, 1995]. To reduce data noises and the aliasing effect caused by the uneven along-track and cross-track data spacings, we applied a Gaussian filter with a full window width of 300 km (see *Wessel and Smith* [1995] for these definitions) to the gridded dynamic heights.

[6] The resulting relative dynamic heights and geostrophic fields at a 10-day interval over the STCC can be seen at the World Wide Web (WWW) page at http://space. cv.nctu. edu.tw/KUDEX/menu.html. These maps on this web page show rich structures of eddy fields and their evolutions. As a summary of eddy dynamics, Figure 1 shows the monthly eddy kinetic energy (EKE) over the STCC from 7 years of T/P altimeter data. EKE is defined as

$$K_e = \frac{1}{2}\left(u^2 + v^2\right) \tag{3}$$

which is a descriptor of eddy dynamics. Figure 1 shows a zonal band between 20°N and 24°N that contains relatively large EKE. This zonal band is baroclinically instable and is therefore eddy-productive [*Qiu*, 1999]. Furthermore, along this band EKE is relatively high in summer and autumn (from June to November), and is relatively low in winter and spring (from December to May).

[7] *Zhang et al.* [2001] and *Kobashi and Kawamura* [2002] show that there is a 90 to 100-day oscillation of sea surface that is associated with eddies over the STCC. *Chelton and Schlax* [1996] and *Liu et al.* [2001], among others, have identified Rossby waves using dynamic heights similar to those used in this paper. To see sea surface variability over the STCC, we computed a time series of SLA averaged over the area 22°N–24°N and 122°E–124°E, which is shown in Figure 2. Also shown in Figure 2 is the spectrum of SLA. In Figure 2 we do see a 90 to 100-day components (the 3 to 4 cycle/year components), but these components are not the dominant components in terms of magnitude. The strongest components in the SLA time series in Figure 2 are the annual and semi-annual components, which originate from Sun's seasonal motion and monsoonal wind, respectively. There is also an interannual component in the SLA, which we believe is correlated with El Niño–Southern Oscillation (ENSO) due to STCC's close location to the warm pool northeast of Australia where warm water is piled up before an El Niño occurs [*Hwang and Chen*, 2000b].

3. Method for Determination of Eddy Kinematic Properties

[8] We used the contours of dynamic heights and the geostrophic velocity fields to identify eddies over the

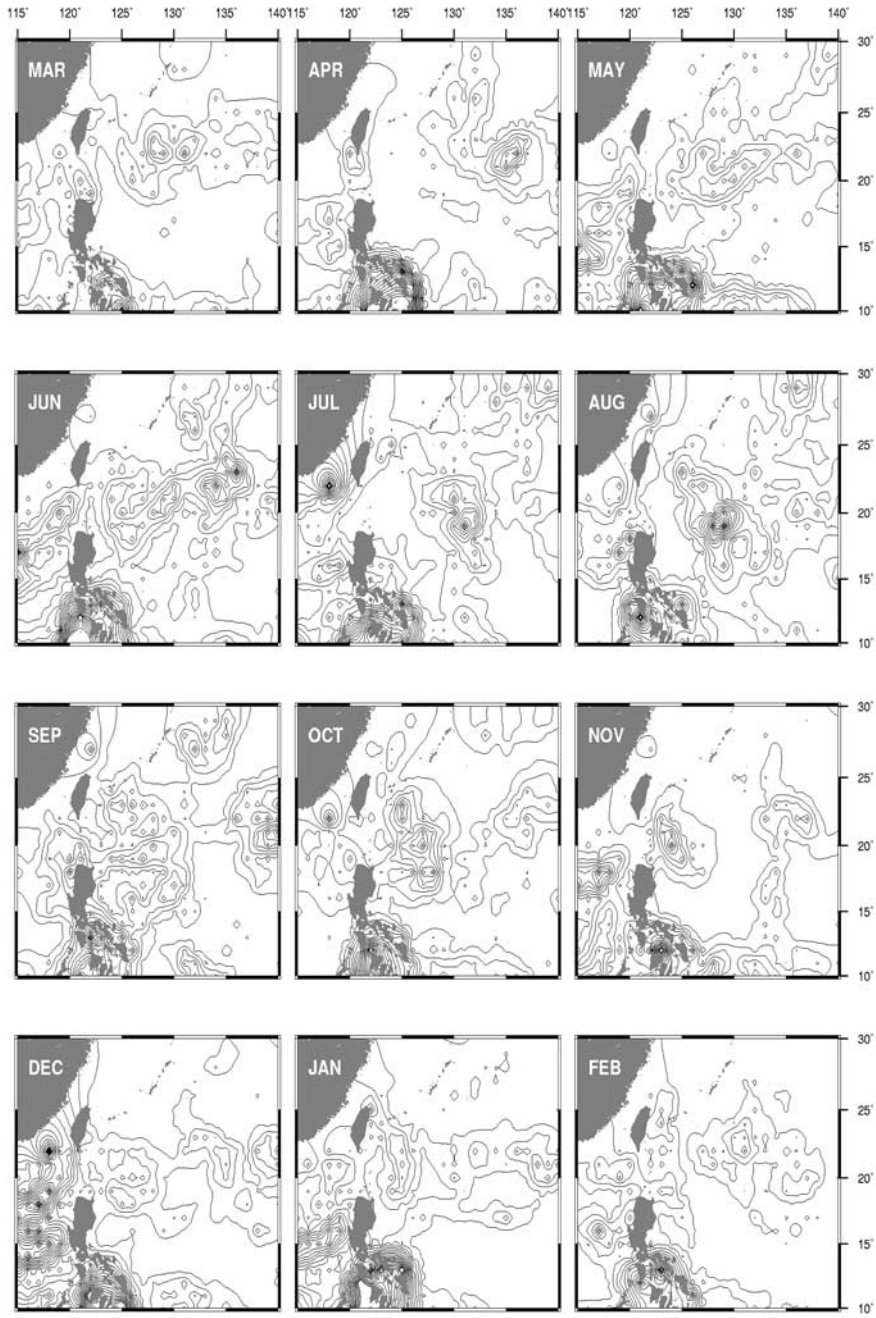

Figure 1. Averaged monthly relative dynamic heights and geostrophic velocities (vectors) over the STCC. Contour interval is 5 $cm^2\ s^{-2}$.

STCC, as was done in *Hwang and Chen* [2000a]; other relevant techniques of eddy identification can be found in, e.g., *Gründlingh* [1995], *Siegel et al.* [1999]. Methods for automatic extraction of features like eddies are, e.g., wavelet decomposition and gradient analysis [*Förstner*, 2000]. However, it will be difficult even if possible to use automatic methods to identify eddies over the STCC due to the complex ocean-land boundaries here. In this paper we adopted the 5-cm contour line in dynamic height as the edge of an eddy, and then estimated the coordinates of its center and radius. The type of an eddy (cyclonic or anticyclonic) is determined by visual inspection of the rotational directions. The acceptance of this eddy, as well as the determination of the eddy's kinematic properties, will be made in the least squares methods described below. Furthermore, the 280-km cross-track spacing of T/P is indeed very coarse and cannot yield eddies with radii similar to those of the first internal deformations. However, considering the ongoing constellation of altimeter satellites formed by ERS-2, ENVISAT, T/P, Jason-1 and Geosat-Follow-On (GFO), we may properly combine altimeter data from these missions to detect internal deformations of small radii. The proposed Wide-Swath Ocean Altimeter (WSOA) [*Fu*, 2003] may also deliver SSHs that fit such a need.

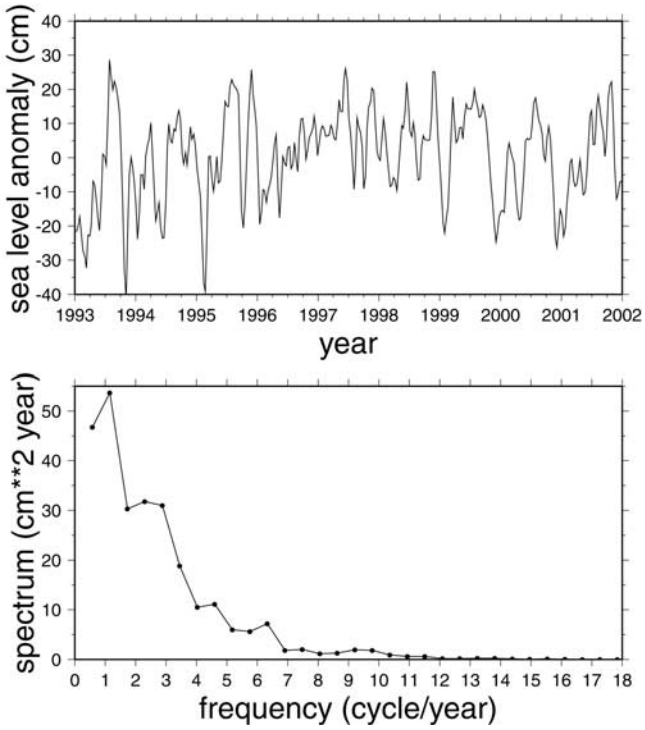

Figure 2. Time series of sea level anomaly east of Taiwan (top) and its spectrum.

[9] To see how an eddy evolves over the STCC, we modify the approach of *Sanderson* [1995] to compute its center velocity, vorticity and deformation rates. First, in a local Cartesian x, y coordinate system, the gradients of geostrophic velocity components are

$$g_{11} = \frac{\partial u}{\partial x}, g_{12} = \frac{\partial u}{\partial y}, g_{21} = \frac{\partial v}{\partial x}, g_{22} = \frac{\partial v}{\partial y} \tag{4}$$

Within a 10-day period, it is assumed that g_{11}, g_{12}, g_{21} and g_{22} are constants with respect to location and time. Using these gradients, we can determine the vorticity by

$$\Omega = g_{21} - g_{12} \tag{5}$$

the shearing deformation rate by

$$\gamma_1 = g_{21} + g_{12} \tag{6}$$

the stretching deformation rate by

$$\gamma_2 = g_{11} - g_{22} \tag{7}$$

and finally the divergence by

$$\psi = g_{11} + g_{22} \tag{8}$$

The vorticity defined in (5) is twice the angular velocity. By definition, in the northern hemisphere the vorticity is positive for a cyclonic (cold-cored, or low-pressure) eddy, and is negative for an anticyclonic (warm-cored, or high-pressure) eddy. Regarding an eddy as a single point, the definitions of shearing and stretching deformation rates are the same as those defined in the geophysical literature dealing with surface deformation; see *Rikitake* [1976] and *Lambeck* [1988]. Also, the total deformation rate of an eddy is $\gamma = \sqrt{\gamma_1^2 + \gamma_2^2}$ [*Carton*, 2001, p. 220].

[10] A positive/negative stretching deformation rate indicates extension/compression in the west-east direction and compression/extension in the south-north direction. In the case of a positive stretching deformation rate, a circular eddy turns to an ellipse with the semi-major axis lying in the west-east direction. Furthermore, a positive/negative shearing deformation rate indicates extension/compression in the northeast-southwest direction and compression/extension in the northwest-southeast direction. Similarly, if the shearing deformation rate is positive, then a circular eddy becomes elliptical with the semi-major axis lying in the northeast-southwest direction. Furthermore, assuming that the variation of vertical velocity of eddy is zero, the continuity equation becomes [*Apel*, 1987, p.101]

$$\nabla \cdot \mathbf{u} = \frac{\partial u}{\partial x} + \frac{\partial v}{\partial y} = g_{11} + g_{22} = 0 \tag{9}$$

[11] Thus a zero divergence implies that the fluid of the eddy follows the continuity equation or the loss of fluid per unit volume per unit time is zero. For a circular, cyclonic eddy, the velocity components within this eddy are

$$\begin{aligned} u &= -\omega y + u_c \\ v &= -\omega x + v_c \end{aligned} \tag{10}$$

where u_c, v_c are instantaneous velocity components of the eddy center relative to the ambient fluid, ω is the angular velocity of the circular eddy. Thus $g_{11} = \partial u/\partial x = g_{22} = \partial v/\partial y = 0$, and $\partial u/\partial y = -\partial v/\partial x = -\omega$, which leads to vorticity = 2ω, shearing deformation rate = stretching deformation rate = divergence = 0.

[12] The velocity of a particle at any location within an eddy is expressed as the sum of the instantaneous center velocity and the incremental velocity due to velocity gradients, that is,

$$u_i + e_{u_i} = g_{11}[x_i - x_0] + g_{12}[y_i - y_0] + u_c, i = 1, \ldots, n \tag{11}$$

$$v_i + e_{v_i} = g_{21}[x_i - x_0] + g_{22}[y_i - y_0] + v_c, i = 1, \ldots, n \tag{12}$$

where u_i, v_i are velocity components of particle, e_{u_i}, e_{v_i} are residuals of velocity components, x_i, y_i are coordinates of particle, x_0, y_0 are coordinates of eddy center and n is number of data points. The kinematic parameters of an eddy to be estimated are g_{11}, g_{12}, g_{21}, g_{22}, x_0, y_0, u_c and v_c. In comparison to the model of *Hwang and Chen* [2000a], the model in (11) and (12) takes into account the instantaneous velocity of the eddy center, which must be considered in view of the westward propagation of eddy, see also *Cushman-Roisin et al.* [1990]. In the practical computations, a preliminary radius of a given eddy is estimated from the dynamic height field. The velocity components u_i, v_i in (11) and (12) are sampled on a $0.25^\circ \times 0.25^\circ$ grid within the eddy, which is defined to be a circular area of the preliminary radius. We used the least squares method to solve for the kinematic parameters. Because (11) and (12)

are nonlinear with respect to the kinematic parameters, it is necessary to use iterations in the least squares estimation. Let vector $\boldsymbol{\beta} = [g_{11}g_{12}g_{21}g_{22}x_0y_0u_cv_c]^{\mathrm{T}}$ contain the kinematic parameters and

$$\boldsymbol{\beta} = \boldsymbol{\beta}_0 + \boldsymbol{\Delta\beta} \tag{13}$$

where vector $\boldsymbol{\beta_0}$ contains the approximate values and vector $\boldsymbol{\Delta\beta}$ contains the corrections to $\boldsymbol{\beta_0}$. Expanding (11) and (12) into a Taylor series and retaining only the first-order terms, we obtain in a matrix representation

$$\mathbf{V} = \mathbf{A\Delta\beta} - \mathbf{L} \tag{14}$$

where $\mathbf{V}$ is a vector containing e_{u_i} and e_{v_i}, $\mathbf{A}$ is the design matrix, and $\mathbf{L}$ is a vector containing u_i, v_i. Specifically, the elements in $\mathbf{V}$, $\mathbf{A}$, and $\mathbf{L}$ are

$$\mathbf{V} = [e_{u_1}e_{v_1}\ldots e_{u_n}e_{v_n}]^T \tag{15}$$

$$A = \begin{bmatrix} x_1 - x_0^0 & y_1 - y_0^0 & 0 & 0 & -g_{11}^0 & -g_{12}^0 & 1 & 0 \\ 0 & 0 & x_1 - x_0^0 & y_1 - y_0^0 & -g_{21}^0 & -g_{22}^0 & 0 & 1 \\ \vdots & \vdots & \vdots & \vdots & \vdots & \vdots & \vdots & \vdots \\ x_n - x_0^0 & y_n - y_0^0 & 0 & 0 & -g_{11}^0 & -g_{12}^0 & 1 & 0 \\ 0 & 0 & x_n - x_0^0 & y_n - y_0^0 & -g_{21}^0 & -g_{22}^0 & 0 & 1 \end{bmatrix} \tag{16}$$

$$\mathbf{L} = \begin{bmatrix} u_1 - u_1^0 & v_1 - v_1^0 & \cdots & u_n - u_n^0 & v_n - v_n^0 \end{bmatrix}^T \tag{17}$$

where g_{11}^0, g_{12}^0, g_{21}^0, g_{22}^0, x_0^0, y_0^0, u_c^0 and v_c^0 are the approximate values of the kinematic parameters, u_i^0 and v_i^0 are the computed velocities obtained by substituting the approximate values into (11) and (12); see, e.g., also *Hwang and Chen* [2000a] for the detail of computing $\boldsymbol{\beta_0}$. The instantaneous velocity components u_c, v_c are taken to be zero initially.

[13] By minimizing the inner-product of $\mathbf{V}$, i.e., $\mathbf{V^TV}$, we obtain the least squares solution of $\boldsymbol{\Delta\beta}$ (cf: *Koch*, 1987):

$$\boldsymbol{\Delta\beta} = \left(\mathbf{A^TA}\right)^{-1}\mathbf{A^TL} \tag{18}$$

which is to be added to the approximate vector $\boldsymbol{\beta_0}$ to yield a new estimate of $\boldsymbol{\beta}$. The estimation is then iterated, and a convergence is reached only when $\boldsymbol{\Delta\beta} \approx \mathbf{0}$. It was found that we may reach $\Delta\beta_i/\beta_i \approx 10^{-7}$ after about three iterations, where $\Delta\beta_i$ and β_i are the elements of vectors $\boldsymbol{\Delta\beta}$ and $\boldsymbol{\beta}$, respectively. The standard errors of the estimated parameters are from the diagonal elements of the following error covariance matrix:

$$\sum\nolimits_{\beta} = \hat{\sigma}^2\left(\mathbf{A}^T\mathbf{A}\right)^{-1} \tag{19}$$

where $\hat{\sigma}^2 = \mathbf{V}^T\mathbf{V}/(n - 8)$.

Table 1. Statistics of T/P-Derived Eddies Over the STCC From 24 March 1995 to 16 October 2000[a]

	Visually Estimated	Model-Selected	Rejection Rate, %
No. of anticyclonic eddies	707	542	23.34
No. of cyclonic eddies	562	381	32.21
Total	1269	923	27.27

[a]T/P, TOPEX/Poseidon; STCC, Subtropical Countercurrent; No., number.

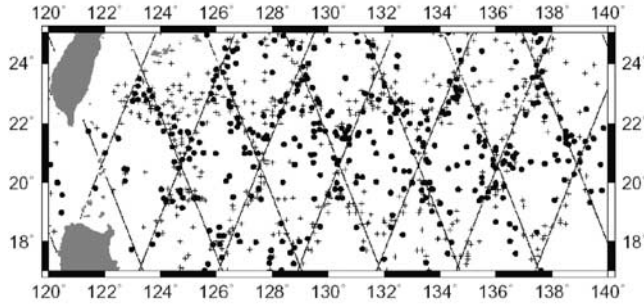

Figure 3. Distribution of cyclonic eddies (crosses) and anticyclonic eddies (circles) found using T/P altimeter data (dotted lines) over the period March 24, 1995 to 16 October 2000.

4. Statistics of Eddies Over the STCC

[14] We have identified eddies over the STCC from March 24, 1995 to October 16, 2000 using T/P-derived dynamic heights and geostrophic fields. Table 1 shows the numbers of visually estimated and model-selected eddies. The visually estimated eddies are based on visual inspections of the dynamic height contours and the geostrophic fields, while the model-selected eddies are determined using the model in (11) and (12) and the least squares solutions. The rejection rate is defined as one minus the ratio between the number of the model-selected eddies and the number of the visually estimated eddies. A visually estimated eddy will survive the model test only when (a) the normal matrix in the least squares solution is positive definite, (b) the iteration in the least squares solution converges and (c) the estimated vorticity matches the type of eddy (positive and negative for cyclonic and anticyclonic eddies, respectively). The rejection rates for both cyclonic and anticyclonic eddies are about 1/4, so the model and the least squares solutions effectively remove bad visually estimated eddies.

[15] Figure 3 shows the distributions of cyclonic and anticyclonic eddies over the STCC. These eddies are relatively dense over a zonal band at around 22°N–23°N. The distribution of eddies is concentrated around the T/P ground tracks. The crossovers of the ascending and descending T/P tracks happen to occur near 22 N, thus the T/P track pattern is ideal for identifying eddies at latitudes around 22 N. Because the two-dimensional SLA fields are filtered by the Gaussian filter with a 300-km wavelength (see Section 2), eddies with diameters less than 300 km cannot be identified here. Furthermore, the averaged cross-track spacing T/P over the STCC is 290 km, thus, if an eddy has a diameter of about 300 km and its center happens to be located at the middle of the parallelogram formed by four T/P tracks, this eddy may

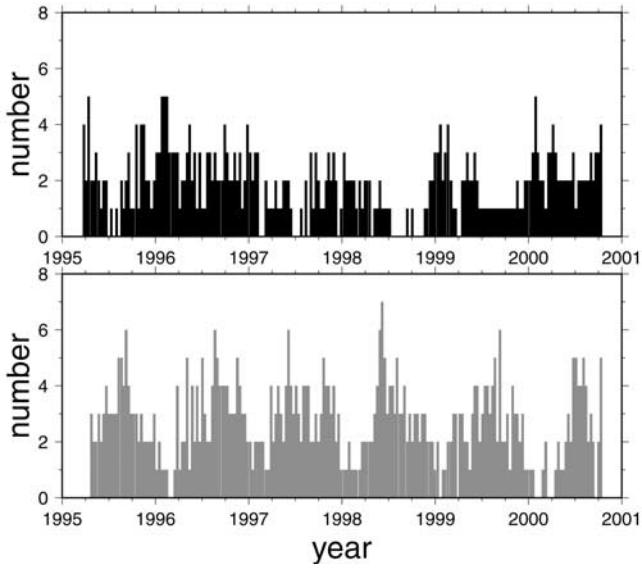

Figure 4. Numbers of cyclonic eddies (top) and numbers of anticyclonic eddies over the STCC.

not be seen in the SLA field. We also identified eddies over the South China Sea (SCS) using T/P altimetry. It is found that, from March 24, 1995 to October 16, 2000, the total numbers of cyclonic eddies over the STCC and the SCS are 381 and 94, respectively, while the numbers of anticyclonic eddies over these two areas are 542 and 124, respectively. Considering that these two areas have about the same size (the area of the STCC over 120 E–140°E, 17 N–25 N is 1,846,892 km^2, and the area of the SCS with depth >200 meters is 2,331,000 km^2), the STCC is indeed an eddy rich zone and this agrees with the finding of *Roemmich and Gilson* [2001].

[16] Figure 4 shows a time series of eddy numbers. In this time series the vertical coordinate is the number of eddies in one T/P 10-day epoch. In general, in summer anticyclonic eddies prevail, while in winter cyclonic eddies are dominant. On average the number of anticyclonic eddies is 1.35 times of the number of cyclonic eddies. During 1997–1998, the number of cyclonic eddies is relatively small compared to other years, and the difference between the numbers of cyclonic and anticyclonic eddies is also small. In the summer of 1998, which is the year after the 1997–1998 El Niño, there is virtually no cyclonic eddy.

[17] Table 2 shows the statistics of eddy kinematic parameters over the STCC. The averaged vorticity of the cyclonic eddies is about 1.66 μ rad s^{-1}, which agrees well with the magnitude of the mean vorticity of the anticyclonic eddies (1.47 μ rad s^{-1}). Interestingly, the mean vorticities of cyclonic and anticyclonic eddies over the SCS are 1.68 and -1.74 μ rad s^{-1}, which are close to those of the eddies over the STCC. On average the deformations and divergences of both cyclonic and anticyclonic eddies are several orders of magnitude smaller than the vorticities.

5. Case Study

5.1. Observing an Anticyclonic Eddy

[18] Anticyclonic eddies are shown to disturb Kuroshio's volume transport and flow directions, and have been studied extensively in, e.g., *Zhang et al.* [2001] and *Takuji et al.* [2002]. Here we first do a case study for an anticyclonic eddy and then for a cyclonic eddy in the next section. Figure 5 shows the profiles of dynamic height associated with an anticyclonic eddy at longitudes 122°E–140°E and at a fixed latitude = 22°N, with the time spanning from October 29, 1996 to July 14, 1997. For convenience this eddy is named Eddy 155–177 (because it is identified using T/P data from cycles 155 to 177). Furthermore, Figure 6 displays successive motions of Eddy 155–177 at a 10-day interval using the contours of dynamic height. On about October 29, 1996, the periphery of Eddy 155–177 was visible near 140°E. It then moved westward to be completely inside the STCC on about November 18, 1996. While propagating, the shape and the size of Eddy 155–177 vary and it is mostly not circular. From December 17, 1996 on, Eddy 155–177 was free from the influence of other water mass, and its shape became nearly circular. On April 25, 1997, Eddy 155–177 met another anticyclonic eddy and its speed became nearly zero. On June 4, 1997, Eddy 155–177 merged with another eddy to form a new eddy; this new eddy disappeared all together later. The averaged propagating speed is 8.3 km day^{-1}. In total, Eddy 155–177 travels a distance of 1814 km in 218 days over the STCC.

[19] To verify Eddy 155–177, we obtained sea surface temperature anomaly (SSTA) from Integrated Global Ocean Services System (IGOSS) at the World Wide Web site http://ingrid.ldeo.columbia.edu/SOURCES/.IGOSS/.nmc/.Reyn_SmithOIv1/.weekly. The SSTA data at IGOSS are on a 1° × 1° grid and are a combination of in-situ measurements and temperatures derived from the Advanced Very High Resolution Radiometer (AVHRR) of the National Oceanic and Atmospheric Administration (NOAA). The SSTA grids were constructed from scattering temperature data by an optimal interpolating scheme; see also *Reynolds and Smith* [1994]. Figure 7 shows a sequence of SSTA images and contours at a 7-day interval from November 27, 1996 to January 22, 1997, overlapping 63 days with the T/P dynamic heights in Figure 6. The SSTA in Figure 7 show moving local highs at about the same locations of Eddy 155–177. The temperature near the eddy center is about 0.5°C higher than the temperature of the surrounding water. If we regard the zero-contour in Figure 7 as the edge of Eddy 155–177, then the estimated radii are about 200–300 km, similar to those shown in Figure 6. Both the dynamic heights in Figure 6 and the SSTA in Figure 7

Table 2. Statistics of the Kinematics of Eddies Over KUDEX From 24 March 1995 to 16 October 2000[a]

	Mean	Minimum	Maximum
	Cyclonic Eddies		
Vorticity	1.657577	0.068	5.236
Shearing deformation	−0.01347	−3.074	2.538
Stretching deformation	0.031058	−2.144	2.93
Divergence	0.001539	−0.417	0.722
	Anticyclonic Eddies		
Vorticity	−1.47259	−4.589	−0.03
Shearing deformation	0.03925	−1.948	2.326
Stretching deformation	−0.00483	−1.968	1.832
Divergence	−2.5E-05	−0.673	0.404

[a]Unit: 1 × 10^{-6} rad s^{-1}; KUDEX, Kuroshio Upstream Dynamics Experiment.

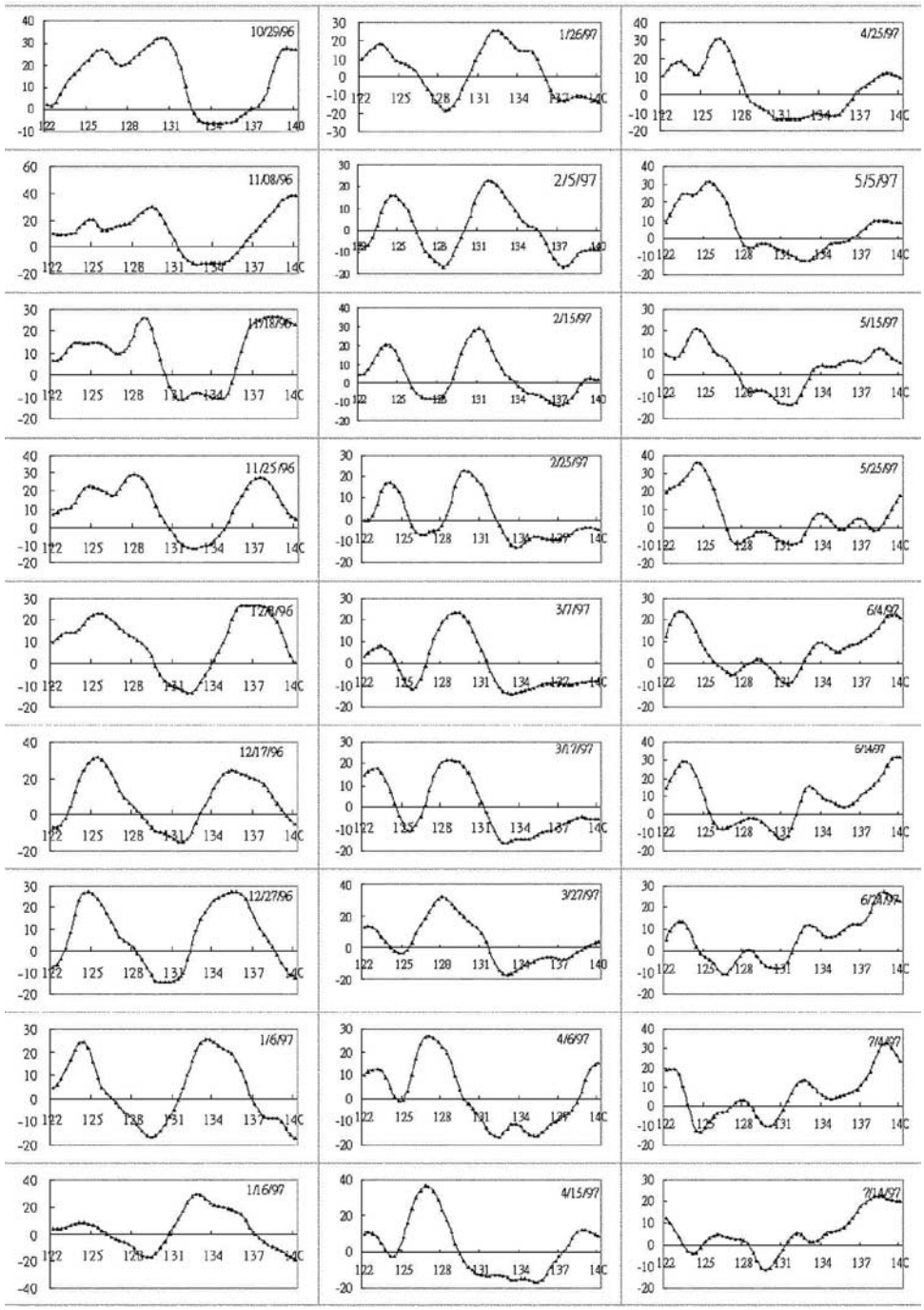

Figure 5. Profiles of dynamic height (vertical axis, unit is cm) associated with Eddy 155–177 at latitude 22°N, from longitude 122°E to 140°E (horizontal axis).

show that the center of Eddy 155–177 was located at about latitude = 23 N and longitude = 137.5°E on November 27, 1996, and the center moved to latitude = 23°N and longitude = 133.5°E on January 22, 1997. This leads to an averaged propagating speed of about 7 km day^{-1} for Eddy 155–177. This estimate is slightly smaller than 8.3 km day^{-1} from the dynamic heights, and the difference may have been due to use of different time spans. Furthermore, Figure 7 shows a band of temperature high along the path of the Kuroshio east of Taiwan. Here the temperature is about 0.5–1°C higher than the surrounding water.

[20] For a further verification we obtained drifter data from the WWW site of the Marine Environmental Data Service (MEDS), Canada (http://www.meds-sdmm.dfo-mpo.gc.ca/meds/Prog_Int/WOCE/WOCE_SVP/SVP_PS_e.htm). The drifter data contain latitudes, longitudes, velocities, temperatures and other information. It is found that the duration time of Drifter 22076 overlapped with that of Eddy 155–177. Because both Drifter 22076 and Eddy 155–177 are in slow motion, a longer (more than 10 days) time span of T/P-derived velocity field is needed in order to see whether Drifter 22076 enters Eddy 155–177. It turns out

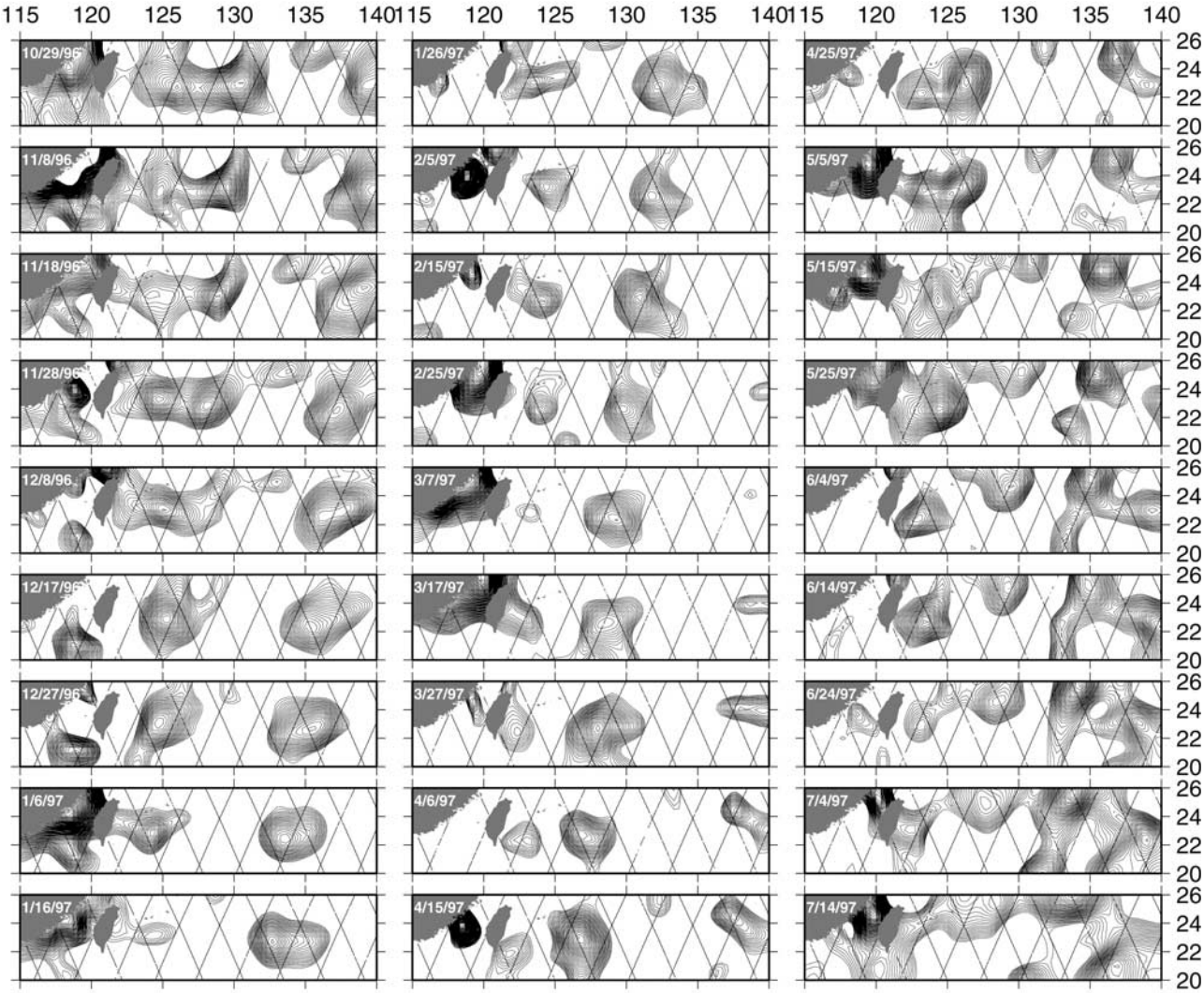

Figure 6. Contours of dynamic height associated with Eddy 155–177 at a 10-day interval from 29 October 1996 to 14 July 1997. Contour interval is 1 cm. Only absolute values greater than 5 cm are plotted. Dotted lines show T/P tracks.

that we need to average velocity fields over January 18, 1997 to March 22 in order to see a complete overlap between Eddy 155–177 and Drifter 22076, as shown in Figure 8. As seen in Figure 8, Drifter 22076 moved along the edge of Eddy 155–177. After entering Eddy 155–177, Drifter 22076 did not stay in this eddy for the rest of its lifetime, rather it left Eddy 155–177 after completing nearly a revolution.

[21] Figure 9 shows the radii, the center coordinates and propagating velocities of Eddy 155–177 at a 10-day interval; the mean values and variabilities of the kinematic parameters of Eddy 155–177 are given in Table 3. From Figure 9 and Table 3, Eddy 155–177 propagated westward in a narrow zonal band centering at 22.629°N. The averaged radius of Eddy 155–177 is 273 km. At the times corresponding to cycles 155 to 157, 163 to 166 and 170 to 174, Eddy 155–177 moved southwestward, and at other times it traveled almost westward. Basically the propagation of this anticyclonic eddy is consistent with what the theory predicts: an anticyclonic eddy propagates southwestward [*Cushman-Roisin*, 1994].

[22] Figure 10 shows time series of vorticity, shearing deformation rate, stretching deformation rate, and divergence of Eddy 155–177. Because of the structures of the error covariance in (19), it turns out that the standard errors of the vorticities and all deformations are the same [*Hwang and Chen*, 2000a], and they are also plotted in Figure 10. The vorticity remains relatively steady during the propagation and it dropped as Eddy 155–177 approached the east coast of Taiwan. Its divergence is nearly zero and was quite stable during the entire lifetime, indicating little loss of eddy fluid during the propagation. The shearing and stretching deformation rates oscillate around zero and both have about the same magnitudes. A significance test [*Koch*, 1987] using the estimated parameters and the standard errors shows that the all the estimated parameters are significant (or non-zero).

5.2. Observing a Cyclonic Eddy

[23] Here we will present a case study for a cyclonic eddy over the STCC. This cyclonic eddy is named Eddy 244–268 for the same reason as for Eddy 155–177. Figure 11

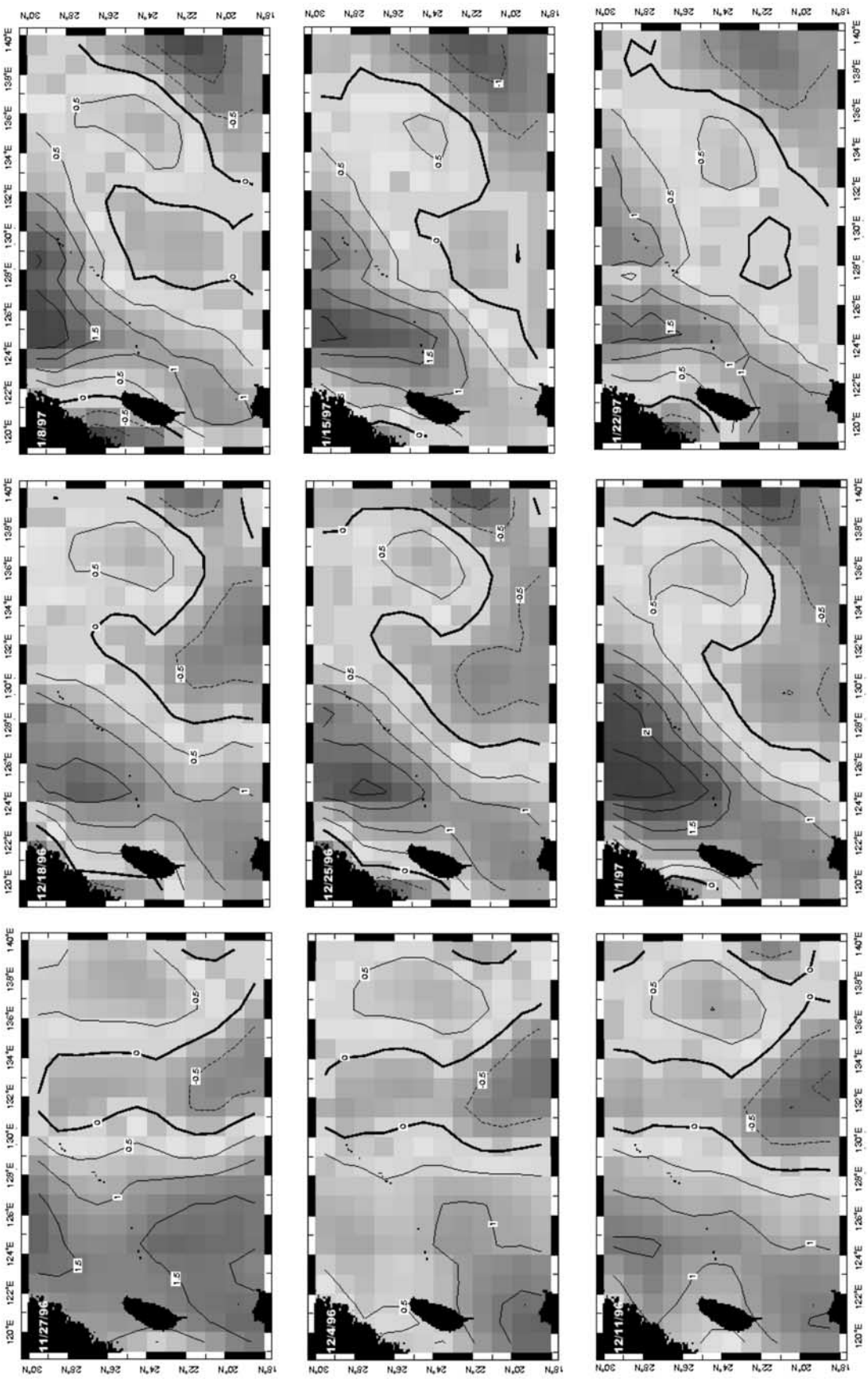

Figure 7. Sea surface temperature anomalies at a 7-day interval from 27 November 1996 to 22 January 1997, corresponding to Eddy 155–177. See color version of this figure in the HTML.

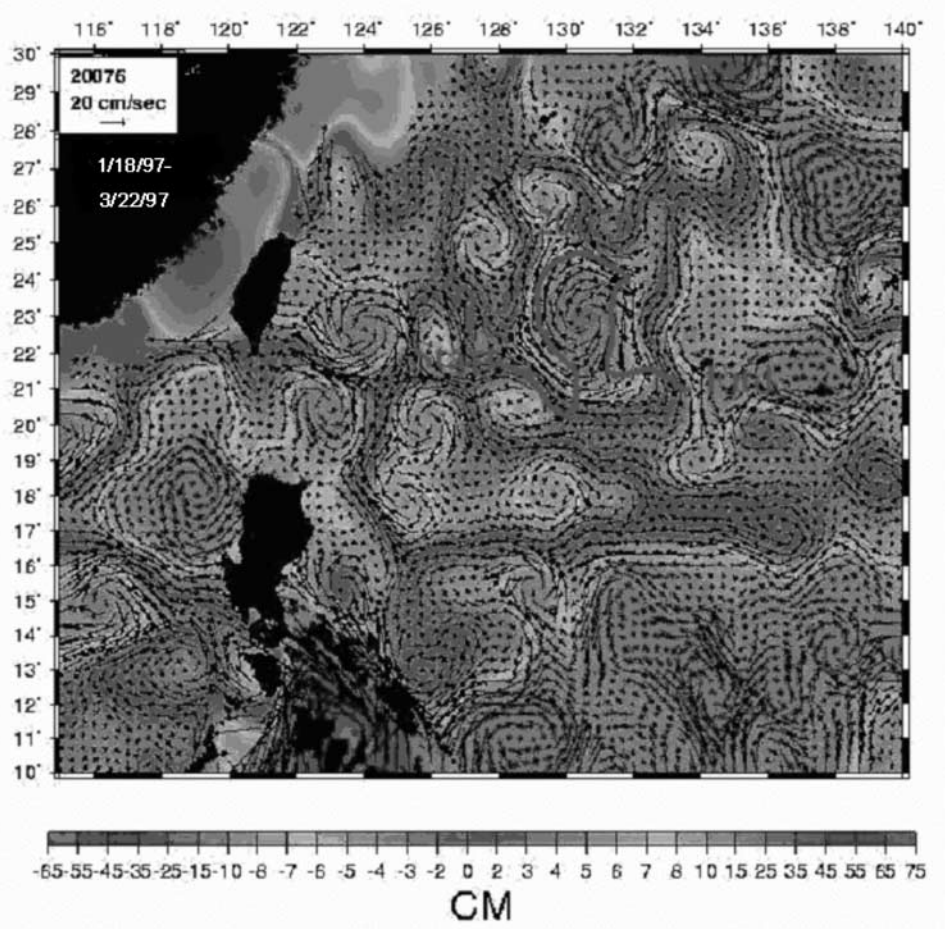

Figure 8. The trace of Drifter 22076 (solid circles) and the averaged geostrophic field and dynamic heights over 16 January 1997 to 17 March 1997 associated with Eddy 155–177. See color version of this figure in the HTML.

shows the contours of dynamic height associated with Eddy 244–268 at a 10-day interval from March 20, 1999 to January 2, 2000. The first sign of this cold-cored eddy occurred on March 30, 1999 and its radius was small. This eddy became full-fledged 90 days later (on May 9, 1999), and then it began to move westward. Like the warm-cored eddy in the previous section, the shape and course vary while Eddy 244–268 is in motion. The shapes become particularly irregular when Eddy 244–268 reaches the Kuroshio east of Taiwan. This cyclonic eddy has an averaged propagating speed of 7.6 km day^{-1} and travels a distance of 1816 km in 238 days.

[24] Again we use temperature data to verify Eddy 244–268. As shown in Figure 12a, from July 14, 1999 to August 11, 1999, a negative temperature anomaly appears in the same location as Eddy 244–268. The temperature of Eddy 244–268 is about 0.5–1°C lower than the surrounding water. However, the structure of the negative temperature anomaly is loose and not as solid as the structure of SLA in Figure 11. The signature of negative temperature anomaly disappeared after August 11, 1999 and the temperature data fail to track the propagation of Eddy 244–268. Then, from November 4, 1999 to January 2, 2002, the signature of temperature corresponding to this eddy emerges again. This is perhaps due to cloud cover that restricts the use of AVHRR in tracking Eddy 244–268 continuously. Also, the upper ocean is affected by surface heating, which may mask this cold-cored eddy. As a further verification, Figure 12b shows 10-day successive temperature fields at a depth = 150 m derived from the US Naval Research Lab's (NRL) North Pacific Ocean Nowcast/Forecast System (NPACNFS). NPACNFS is an eddy resolving model that is based on the Princeton Ocean Model (POM). Figure 12b shows successive temperature lows corresponding to Eddy 244–268, thus proving its existence. Interestingly, there is another cyclonic eddy emerging to the east of Eddy 244–268 from November 13, 1999 to January 2, 2002 (see the last 7 maps in Figure 11), which also appears in the temperature images in Figures 12a and 12b. Unfortunately, there are no drifters over the STCC that match exactly the track of Eddy 244–268.

[25] Figure 13 shows radii, center coordinates and propagating velocities of Eddy 244–268. Figure 14 shows the time series of the estimated kinematic parameters and standard errors of Eddy 244–268. Again, a significance test [*Koch*, 1987] using the estimated parameters and standard errors shows that all the estimated parameters are significant (or non-zero). Figures 13 and 14 are to be compared with Figures 9 and 10. We also computed the mean values and variabilities of kinematic parameters for

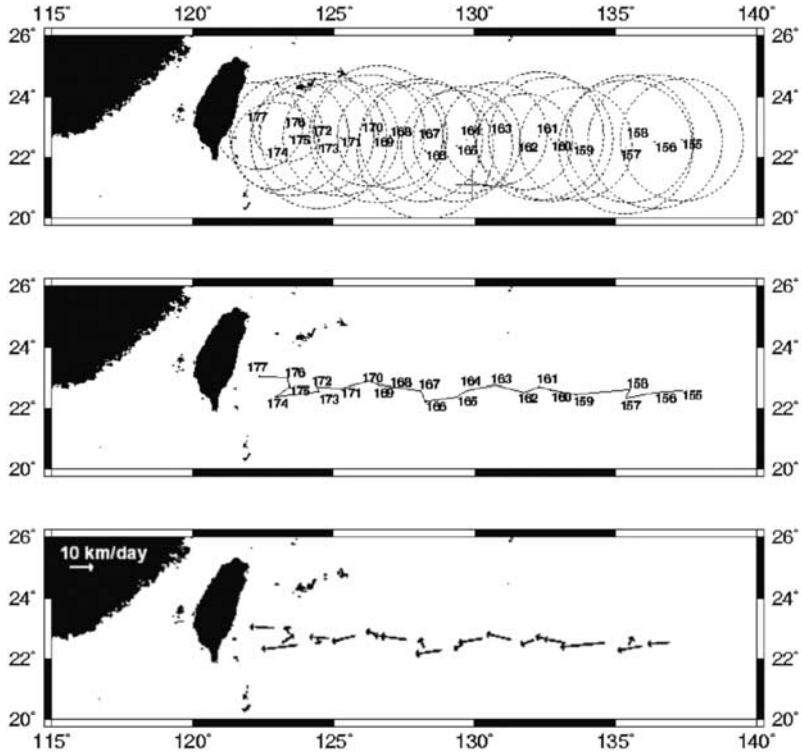

Figure 9. Radii (top), center coordinates (middle, with T/P cycles) and propagating velocities (bottom) of Eddy 155–177.

Eddy 244–268, which are given in Table 3. Compared to Eddy 155–177, Eddy 244–268 has a slightly smaller instantaneous velocity. The vorticity of the cyclonic eddy is also smaller than that of the anticyclonic eddy. From the variabilities of latitude, the propagation of Eddy 244–268 follows a broader zonal band than that of Eddy 155–177. This broader zonal band is clearly seen in Figure 13, which shows that Eddy 244–268 emerged at latitude near 24°N, moved southwestward to 22°N and then moved back to 23°N. Also, Eddy 244–268 has larger shearing deformation rates and stretching deformation rates than those of Eddy 155–177, indicating that the flattening of Eddy 244–268 is larger than that of Eddy 155–177. The averaged radius of the Eddy 244–268 is smaller than that of Eddy 155–177, but the variabilities of the radii of the two eddies are almost the same. Interestingly, the divergence of the cyclonic eddy is an order of magnitude smaller than that of the anticyclonic eddy, although both of them are nearly zero. This means that Eddy 244–268 lost less fluid than Eddy 155–177 during the propagation. Both eddies have larger vorticities when they reached east of Taiwan.

[26] The origins of Eddies 155–177 and 244–268 are clearly due to baroclinic instability. This is shown in *Qiu* [1999] and *Kobashi and Kawamura* [2002]. Theoretical studies of baroclinic instability associated with eddies can be found in, e.g., *Cushman-Roisin* [1994], and *Olascoaga and Ripa* [1999]. *Cushman-Roisin* [1994, p. 227] shows that, in a stratified system, lateral displacements in the geostrophic flow cause vertical stretching and squeezing, which generate a cyclonic vortex or an anticyclonic vortex, or both. Such a vortex will then evolve away from the initial state. Over the STCC, a vortex originating from baroclinic instability will move westward, as demonstrated by the theory of *Nof* [1983] and the T/P observations in this paper.

6. Discussions

6.1. Propagation of Eddies

[27] The propagation mechanism of mesoscale eddies has been discussed by, e.g., *Nof* [1983] and *Cushman-Roisin et al.* [1990; *Cushman-Roisin*, 1994]. As demonstrated by *Cushman-Roisin* [1994, p. 256], the migration of a mesoscale eddy is primarily induced by the varying thickness of the layer surrounding the eddy. This primary effect introduces a westward motion of eddy for cyclonic and anticyclonic eddies in the northern hemisphere. In general, the motion of both Eddy 155–177 and Eddy 244–268 are consistent with such a predicted motion, since in most cases they move westward. Moreover, the warm Eddy 155–177 retreated and migrated northward when reaching 123°E near

Table 3. Mean Values and Variabilities of Kinematic Parameters for Eddy 155–177 and Eddy 244–268

	Eddy 155–177		Eddy 244–268	
Parameters	Mean	Variability	Mean	Variability
Center velocity, km day^{-1}	3.795	1.845	3.181	2.519
Vorticity, μ rad s^{-1}	−2.098	0.633	1.513	0.539
Shearing deformation, μ rad s^{-1}	−0.021	0.314	0.053	0.570
Stretching deformation, μ rad s^{-1}	−0.174	0.367	−0.222	0.376
Divergence, μ rad s^{-1}	0.015	0.046	0.001	0.061
Radius, km	273	42	240	49
Latitude, deg N	22.629	0.200	23.074	0.766

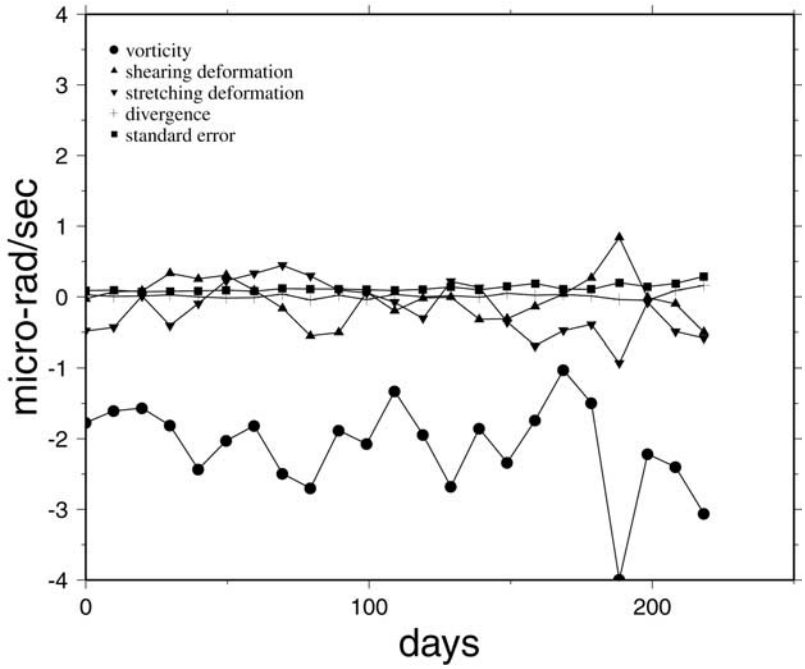

Figure 10. Time series of vorticity, shearing deformation rate, stretching deformation rate, divergence, standard error of vorticity and deformation of Eddy 155–177. Days are counted from 29 October 1996.

a steep bottom slope. This phenomenon has been confirmed by numerical experiments. Based on a primitive equation model, *Itoh and Sugimoto* [2001] show that warm-core rings that initially have baroclinic velocity would move northward while approaching a steep bottom topography of a western boundary.

[28] Another interesting feature of Eddy 244–268 is that it moves southward dramatically at around 130°E

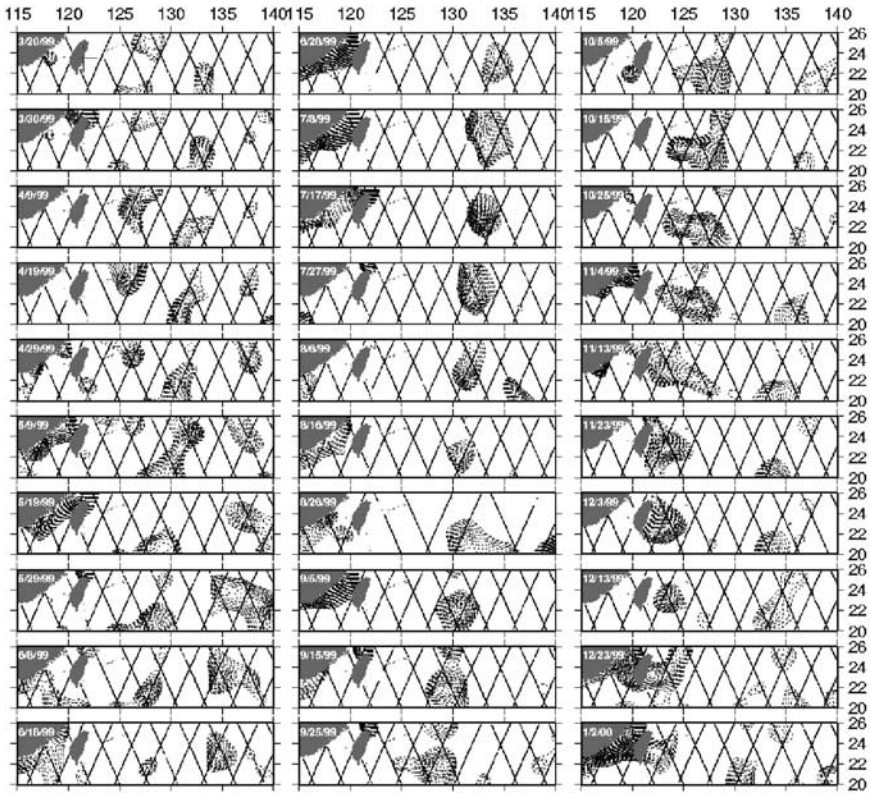

Figure 11. Contours of dynamic height associated with Eddy 244–268 at a 10-day interval from 20 March 1999 to 2 January 2000. Contour interval is 1 cm. Only absolute values greater than 5 cm are plotted. Dotted lines show T/P tracks.

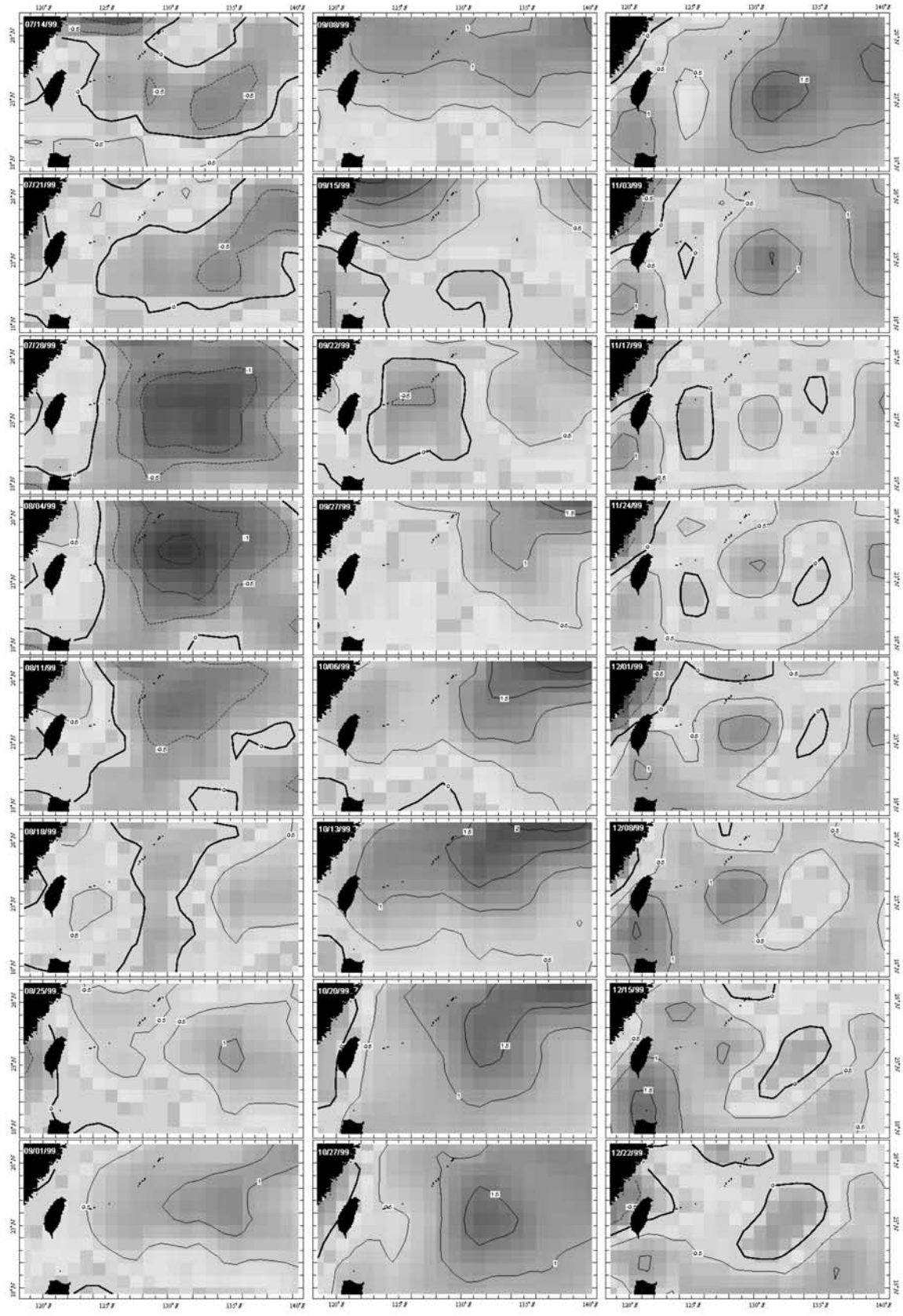

Figure 12. (a) Sea surface temperature anomaly from AVHHR at a 7-day interval. (b) Sea surface temperature from NPACNFS model outputs at times corresponding to T/P repeat cycles. Contour interval is 0.5°C. See color version of this figure in the HTML.

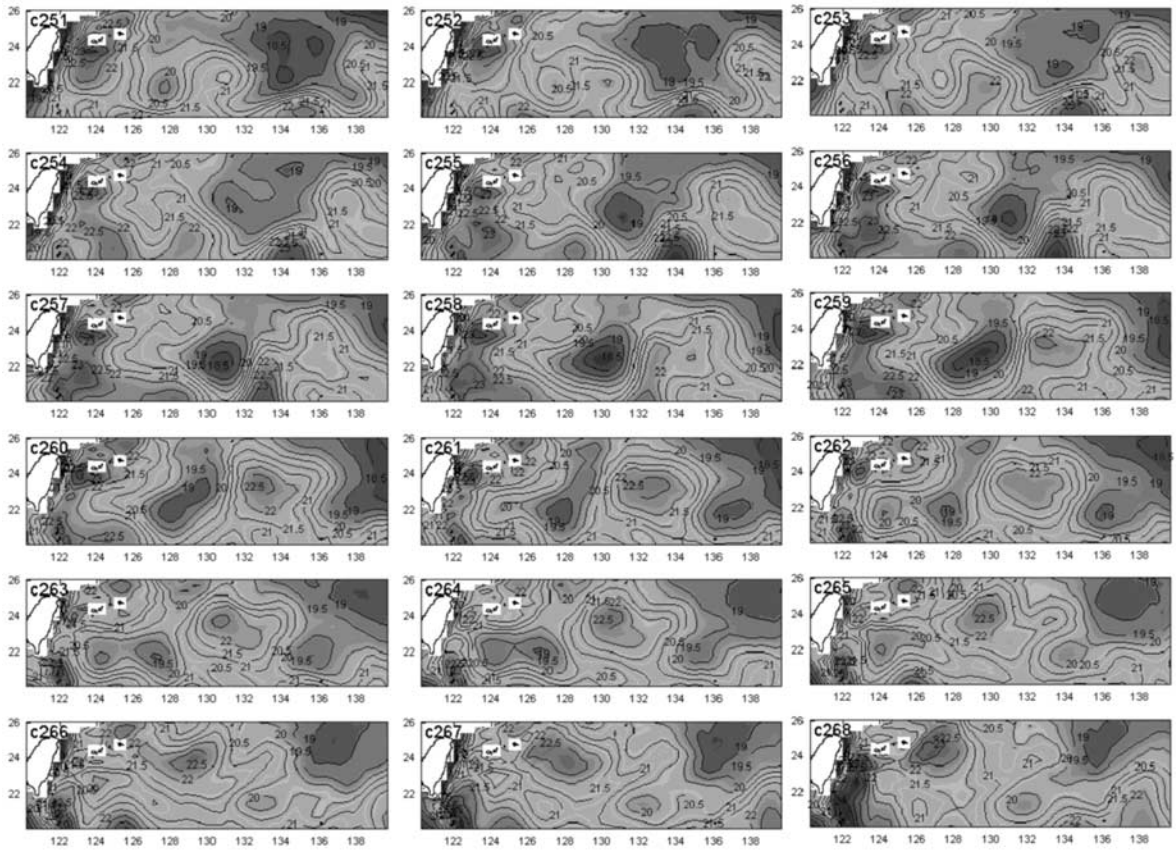

Figure 12. (continued)

(Figure 13), where Eddy 244–268 interacted with a newly formed eddy to the south (Figure 11). Merging and mutual advection between Eddy 244–268 and the new eddy resulted in a southward motion. This merging process also supplied these eddies with energy and vorticity [*Yasuda*, 1995]. This explains why Eddy 244–268 propagated southwest before reaching 130°E and the propagation of this cold eddy around 130°E was temporally not consistent with the theory. As shown in Figure 15, east of 130°E the mean geostrophic flows contain weak southward components which somehow cause this cyclonic eddy to drift southward also. Eddy 244–268 gradually moves northward after merging. *Cushman-Roisin* [1994] predicts that secondary beta gyres originating from the advection of surrounding fluid of an eddy will introduce a northward motion for a cyclonic eddy. Therefore in theory a cyclonic eddy will move westward or northwestward. The northwestward motion of cold Eddy 244–268 again is consistent with the theory of *Cushman-Roisin* [1994].

[29] On the other hand, the observed propagating speeds of the two eddies are larger than the predicted speeds. Such a difference between observation and theory is also found in the propagations of eddies near Hawaii [*Holland and Mitchum*, 2001]. Many factors contribute to the difference between theory and observation, e.g., interaction of eddies, bottom topography, the effect of mean flow, and long wave propagation. Regarding the effect of mean flow, Figure 15 shows the dynamic height from *Levitus et al.* [1997]. Using equations (1) and (2), we computed mean geostrophic flows from the mean dynamic height of *Levitus et al.* [1997], which are also shown in Figure 15. The Kuroshio Current is excluded from the mean flow presented in Figure 15. From Figure 15, the mean geostrophic flows in STCC are very weak (about 2 cm s^{-1}), which should have little effect on the propagation of Eddies 155–177 and 244–268.

[30] The instantaneous center velocities u_c, v_c, which are velocities relative to the ambient fluid, are different from the propagating velocities. For Eddy 155–177, the mean difference between the propagating velocity and the instantaneous center velocity is 4.5 km/day; for Eddy 244–268, the mean difference is 4.3 km/day. These differences are almost identical, suggesting that there must be a stable effect influencing the propagations of the two eddies. Furthermore, the directions of motion in the propagating velocity fields are different from those in the instantaneous center velocity fields, but both have westward velocity components. Obviously the mean flow cannot fully account for the difference between the propagating velocity and the instantaneous center velocity because again the mean flow is too small here. A possible cause of such a difference is Rossby wave. In fact, the averaged propagating velocity of 8 km day^{-1} is quite consistent with the observed velocities of Rossby wave in, e.g., *Chelton and Schlax* [1996], *Dewar* [1998] and *Cipollini et al.* [2000]. Furthermore, *Liu et al.* [2001] has presented a detailed analysis of Rossby waves over the STCC and pointed out a 90-day oscillation in sea

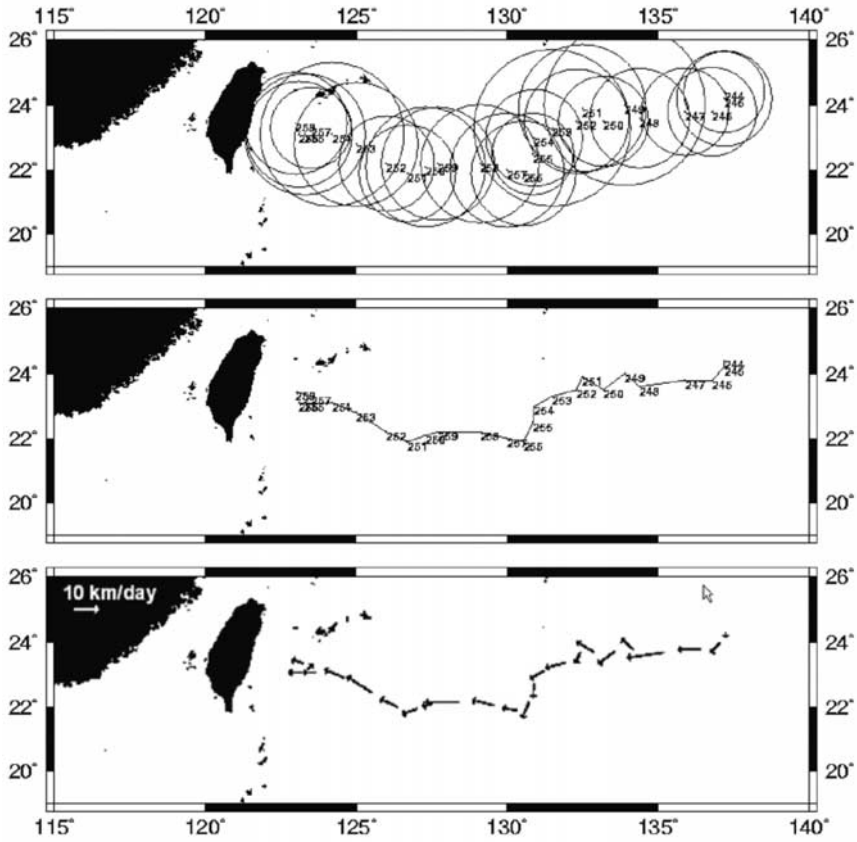

Figure 13. Radii (top), center coordinates (middle, with T/P cycles) and propagating velocities (bottom) of Eddy 244–268.

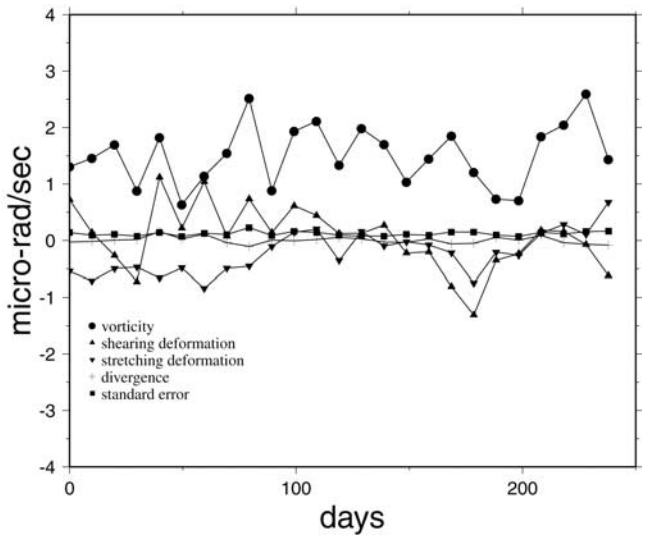

Figure 14. Time series of vorticity, shearing deformation, stretching deformation, divergence, standard errors of vorticity and deformation of Eddy 244–268. Days are counted from 20 March 1999.

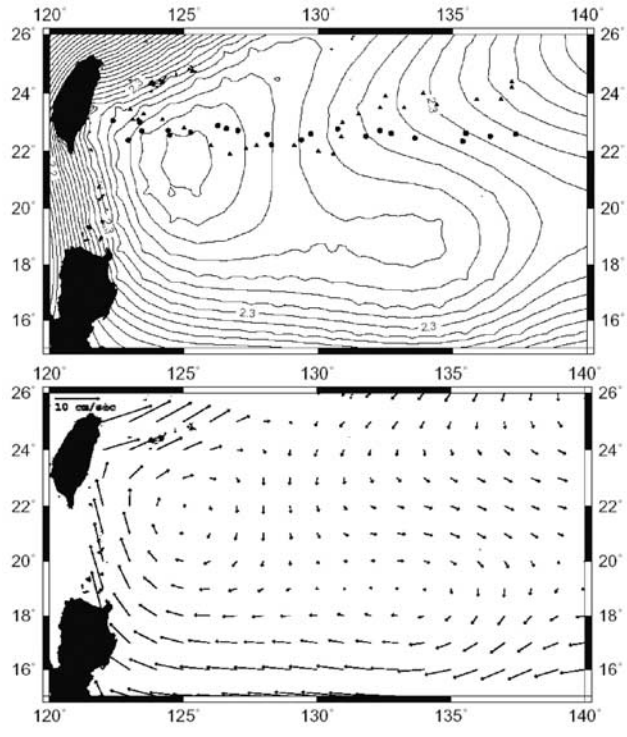

Figure 15. Mean dynamic height (a) and geostrophic velocities from *Levitus et al.* [1997]. Circles and triangles represent the centers of Eddies 155–177 and 244–268, respectively.

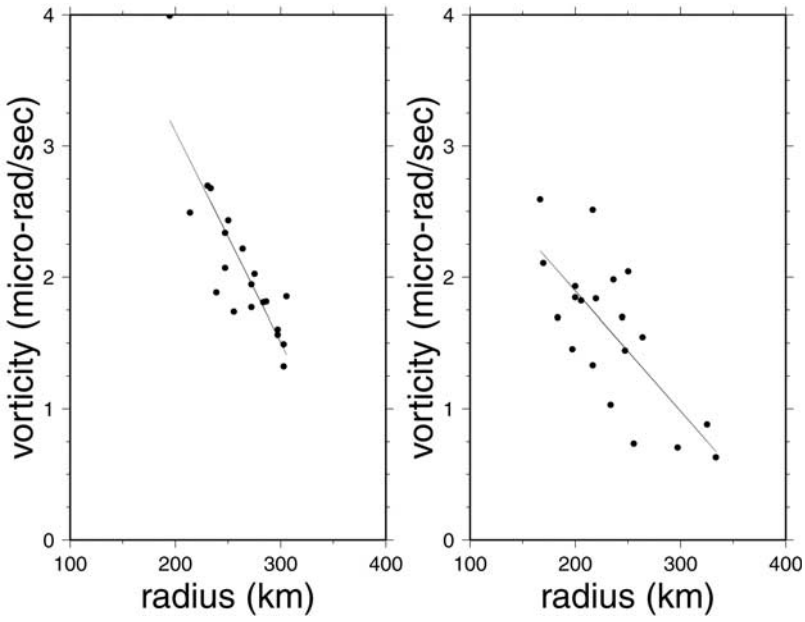

Figure 16. Relationships between radius and vorticity for Eddy 155–177 (left) and Eddy 244–268.

surface height associated with long Rossby wave with wavelengths ranging from 450 to 840 km. That is, Rossby wave occurs about every 90 days and it should have a great consequence on eddies over the STCC. Therefore it is hypothesized that the two eddies under study may happen to "take a ride" on the concurring Rossby waves and the propagating velocities in Figures 11 and 13 are actually the velocities of Rossby waves. Future work should explore this hypothesis by numerical modeling.

6.2. Conservation of Angular Momentum

[31] Figure 16 shows the relationships between vorticity and radius for Eddies 155–177 and 244–268. For Eddy 155–177, a strong linear relationship exists, while for Eddy 244–268 the linear relationship is weaker. The correlation coefficient is −0.87 for Eddy 155–177, and is −0.73 for Eddy 244–268, which are both statistically significant. For these two eddies, the general trend is that vorticity decreases with increasing radius, which obeys the law of conservation of angular momentum. This also shows that the friction between the fluid of eddy and the ambient fluid causes little loss of energy during the propagations of the two eddies. As a summary, we derive the following empirical relationships between vorticity and radius for Eddies 155–177 (anticyclonic) and 244–268 (cyclonic), respectively:

$$v_a = -0.02 r_a + 6.31$$
$$v_c = -0.01 r_c + 3.72 \quad (20)$$

where v_a, v_c are the absolute values of vorticities in μ rad, and r_a, r_c are radii in km.

6.3. Deformations of Eddies

[32] Eddies 155–177 and 244–268 have deformation rates that are non zero in most cases, indicating that their shapes are largely not circular during the propagations and evolutions. This phenomenon can also be seen in Figures 6 and 11. The degree of deformation is proportional to the magnitude of deformation rate. Figures 10 and 14 show that the shearing and stretching deformation rates oscillate around zero. Based on the interpretation of deformation rates in Section 3, the change of sign indicates that the major axes of the two eddies rotate during propagation. The shearing deformation rate of Eddy 244–268 (see Figure 14) oscillates rapidly, suggesting its shape also changes rapidly. Eddy 244–268's stretching deformation rate goes slowly from negative to zero and changes its sign back to negative. When the deformation rate is nearly zero, the shape of an eddy then approaches circle. Figures 10 and 14 show that there is a tendency that the deformation will approach zero. Such a tendency brings the shape from ellipse to circle and is called axisymmetrization [*Carton*, 2001]. Due to the influence of the ambient fluid a circular eddy will be deformed and its shape becomes elliptical again. This process is repeated and that's why we see the deformation rates oscillate around zero in Figures 10 and 14. It is noted that the deforming factors of Eddy 155–177 and 244–268 are not entirely due to the shearing forces from the mean geostrophic flow, which is quite weak here (see Figure 15), see also *Carton* [2001].

7. Conclusions

[33] This paper presents a method for determining the kinematic properties of mesoscale eddies based on the principle of constant velocity gradients and instantaneous center velocity. In such a model, the deformation rates are determined and can be used to see the shape evolution of an eddy during its lifetime. An anticyclonic and a cyclonic eddy are studied using this method and their existences are verified by temperature data and drifter data. This is the first time an anticyclonic and a cyclonic eddy are completely tracked during their lifetimes over the STCC. The two

eddies propagate westward with an averaged speed of about 8 km day^{-1} and their shapes are not circular in most cases. The north-south directions of propagations of the two eddies do not follow exactly what the theories of *Nof* [1983] and *Cushman-Roisin et al.* [1990] have predicted, and the propagation speeds are larger than the theoretical speeds. The mean flow over the STCC is quite weak, so it is not the major cause of the deviation between observation and theory. It is very likely that the two eddies propagate with Rossby waves, which themselves also have speeds larger than what theories have predicted, see, e.g., *Chelton and Schlax* [1996] and *Dewar* [1998]. The estimated kinematic parameters can be used to verify results in an eddy-resolving model of ocean circulation.

[34] **Acknowledgments.** This research is supported by the National Science Council of Taiwan under contract NSC89-2611-M-009-003 -OP2. We are grateful to AVISO for providing the T/P altimeter data, IGOSS for the sea surface temperature data and the Marine Environmental Data Service (MEDS), Canada for the drifter data. Dr. I-Huan Lee helps to obtain temperature fields. The NRL NPACNFS output has been used in the study. We thank two anonymous reviewers for their valuable comments that improved the quality of this paper.

References

Andrade, C. A., and E. D. Barton (2000), Eddy development and motion in Caribbean Sea, *J. Geophys. Res.*, *105*, 26,191–26,201.

Apel, J. R. (1987), *Principles of Ocean Physics*, Academic, San Diego, Calif.

Archivings Validation and Interpretation of Satellite Oceanographic data (AVISO) (1996), *User Handbook for Merged TOPEX/Poseidon Products*, 3rd ed., Cent. Natl. d'Etudes Spatiales, Toulouse, France.

Carton, X. (2001), Hydrodynamical modeling of oceanic vortices, *Surv. Geophys.*, *22*, 179–263.

Chelton, D. B., and M. G. Schlax (1996), Global observations of oceanic Rossby waves, *Science*, *272*, 235–238.

Chu, P. C., and R. F. Li (2000), South China Sea isopycnal-surface circulation, *J. Phys. Oceanogr.*, *30*, 2419–2438.

Cippollini, P., D. Cromwell, G. D. Quartly, and P. G. Challenor (2000), Remote sensing of oceanic extra-tropical Rossby waves, in *Satellites, Oceanography and Society*, edited by D. Halpern, pp. 99–124, Elsevier Sci., New York.

Cushman-Roisin, B. (1994), *Introduction to Geophysical Fluid Dynamics*, Prentice-Hall, Old Tappan, N. J.

Cushman-Roisin, B., E. P. Chassignet, and B. Tang (1990), Westward motion of mesoscale eddies, *J. Phys. Oceangr.*, *20*, 758–768.

Dewar, W. K. (1998), On "too fast" baroclinic planetary waves in the general circulation, *J. Phys. Oceanogr.*, *28*, 1739–1758.

Förstner, W. (2000), Image preprocessing for feature extraction in digital intensity, color and range images, in *Geomatic Methods for the Analysis of Data in the Earth Sciences*, edited by A. Dermanis, A. Grun, and F. Sanso, *Lecture Notes Earth Sci.*, *50*, 165–188.

Fu, L.-L. (2003), Wide-swath altimetric measurement of ocean surface topography, p. B2, Abstract Week A, IUGG 2003, 30 June–11 July, Sapporo, Japan.

Fu, L.-L., and A. Cazenave (Eds.) (2001), *Satellite Altimetry and Earth Sciences*, Academic, San Diego, Calif.

Fu, L.-L., E. J. Christensen, C. A. Yamarone Jr., M. Lefebvre, Y. Ménard, M. Dorrer, and P. Escudier (1994), TOPEX/Poseidon mission overview, *J. Geophys. Res.*, *99*, 24,369–24,382.

Gründlingh, M. L. (1995), Tracking eddies in the southeast Atlantic and southwest Indian Oceans with TOPEX/Poseidon, *J. Geophys. Res.*, *100*, 24,977–24,986.

Holland, L. C., and G. T. Mitchum (2001), Propagation of Big Island eddies, *J. Geophys. Res.*, *106*, 935–944.

Hwang, C., and S.-A. Chen (2000a), Circulations and eddies over the South China Sea derived from TOPEX/Poseidon altimeter data, *J. Geophys. Res.*, *105*, 23,943–23,965.

Hwang, C., and S.-A. Chen (2000b), Fourier and wavelet analyses of TOPEX/Poseidon-derived sea level anomalies over the South China Sea: A contribution to South China Sea Monsoon Experiment, *J. Geophys. Res.*, *105*, 28,785–28,804.

Itoh, S., and T. Sugimoto (2001), Numerical experiments on the movement of a warm-core ring with the bottom slope of a western boundary, *J. Geophys. Res.*, *106*, 26,851–26,862.

Johns, W. E., T. N. Lee, D. Zhang, and R. Rantopp (2001), The Kuroshio east of Taiwan: Moored transport observations from the WOCE PCM-1 array, *J. Phys. Oceangr.*, *31*, 1031–1054.

Kirwan, A. D., Jr., W. J. Merreil Jr., J. K. Lewis, R. E. Whitaker, and R. Legeckis (1984), A model for the analysis of drifter data with an application to a warm core ring in the Gulf of Mexico, *J. Geophys. Res.*, *89*, 3425–3438.

Kobashi, F., and H. Kawamura (2002), Seasonal variation and instability nature of the North Pacific Subtropical Countercurrent and the Hawaiian Lee Countercurrent, *J. Geophys. Res.*, *107*(C11), 3185, doi:10.1029/2001JC001225.

Koch, K. R. (1987), *Parameter Estimation and Hypothesis Testing in Linear Models*, Springer-Verlag, New York.

Lambeck, K. (1988), *Geophysical Geodesy*, Clarendon, Oxford, UK.

Levitus, S., G. I. Monterey, and T. Boyer (1997), Seasonal variability of dynamic height and its Fourier analysis, *NOAA NESDIS Atlas 15*, U.S. Govt. Print. Off., Washington, D. C.

Liu, Q. Y., S. X. Wang, Z. Y. Liu, and H. J. Yang (2001), Dynamic features of long Rossby wave in the north Pacific subtropical countercurrent, *Chin. J. Geophys.*, *44*, 28–37.

Meyers, S. D., and S. Basu (1999), Eddies in the eastern Gulf of Alaska from TOPEX/Poseidon altimetry, *J. Geophys. Res.*, *104*, 13,333–13,344.

Nof, D. (1983), On the migration of isolated eddies with application to Gulf Stream rings, *J. Mar. Res.*, *41*, 399–425.

Okkonen, S. R. (2001), Altimeter observations of Bering Slope Current eddy field, *J. Geophys. Res.*, *106*, 2465–2476.

Okubo, A., and C. C. Ebbesmeyer (1976), Determination of vorticity, divergence, and deformation rates from analysis of drogue observations, *Deep Sea Res.*, *23*, 349–352.

Olascoaga, M. J., and P. Ripa (1999), Baroclinic instability in a two-layer model with a free boundary and β effect, *J. Geophys. Res.*, *104*, 23,357–23,366.

Qiu, B. (1999), Seasonal eddy field modulation of the north pacific subtropical countercurrent: TOPEX/Poseidon observations and theory, *J. Phys. Oceanogr.*, *29*, 2471–2486.

Qiu, B. (2002), Large-scale variability in the midlatitude subtropical and subpolar North Pacific Ocean: Observations and causes, *J. Phys. Oceanogr.*, *32*, 353–375.

Qiu, B., and R. Lukas (1996), Seasonal and interannual variability of the North Equatorial Current, the Mindanao Current, and the Kuroshio along the Pacific western boundary, *J. Geophys. Res.*, *101*, 12,315–12,330.

Reynolds, R. W., and T. M. Smith (1994), Improved global sea surface temperature analyses, *J. Clim.*, *7*, 929–948.

Rikitake, T. (1976), *Earthquake Prediction*, Elsevier Sci., New York.

Roemmich, D., and J. Gilson (2001), Eddy transport of heat and thermocline waters in the north Pacific: A key to interannual/decadal climate variability?, *J. Phys. Oceanogr.*, *31*, 675–687.

Sanderson, B. G. (1995), Structure of an eddy measured with drifters, *J. Geophys. Res.*, *100*, 6761–6776.

Siegel, D. A., D. J. McGillicuddy Jr., and E. A. Fields (1999), Mesoscale eddies, satellite altimetry and new production in the Sargasso Sea, *J. Geophys. Res.*, *104*, 13,359–13,380.

Takuji, W., H. Mitsudera, B. Taguchi, and Y. Yoshikawa (2002), On the eddy-Kuroshio interaction: Evolution of the mesoscale eddy, *J. Geophys. Res.*, *107*(C8), 3088, doi:10.1029/2000JC000756.

Wessel, P., and W. H. F. Smith (1995), New version of the Generic Mapping Tool released, *Eos Trans. AGU*, *76*(46), Fall Meet. Suppl., F329.

Wunsch, C., and D. Stammer (1998), Satellite altimetry, the marine geoid, and the oceanic general circulation, *Annu. Rev. Earth Planet. Sci.*, *26*, 219–253.

Yang, Y. (1999), Mesoscale eddies' influence on the Taiwan Current (Kuroshio) volume transport, Ph.D. thesis, Inst. of Oceanogr., Natl. Taiwan Univ., Taiwan.

Yasuda, I. (1995), Geostrophic vortex merger and streamer development in the ocean with special reference to the merger of Kuroshio warm core rings, *J. Phys. Oceanogr.*, *25*, 979–996.

Zhang, D., T. N. Lee, and W. E. Johns (2001), The Kuroshio east of Taiwan: Modes of variability and relationship to interior ocean mesoscale eddies, *J. Phys.*, *31*, 1054–1074.

C. Hwang, Department of Civil Engineering, National Chiao Tung University, 1001 Ta Hsueh Road, Hsinchu 106, Taiwan. (hwang@geodesy.cv.nctu.edu.tw)

R. Kao, National Space Program Office, 8F, 9, Prosperity 1st Road, Science-Based Industrial Park, Hsinchu 300, Taiwan.

C.-R. Wu, Department of Earth Sciences, National Taiwan Normal University, Taipei, Taiwan. (cwu@cc.ntnu.edu.tw)